



Impact of interannually variable diffuse attenuation coefficients for downwelling irradiance on biogeochemical modelling

Elena Terzić^{a,*}, Stefano Salon^a, Gianpiero Cossarini^a, Cosimo Solidoro^a, Anna Teruzzi^a, Arnau Miró^{a,b}, Paolo Lazzari^a

^a National Institute of Oceanography and Applied Geophysics - OGS, Trieste, Italy

^b Barcelona Supercomputing Center (BSC), Barcelona, Spain

ARTICLE INFO

Keywords:

Marine biogeochemical modelling
Satellite observations
Light extinction coefficient
BGC-Argo observations
Deep chlorophyll maximum
Mediterranean Sea

ABSTRACT

Remotely sensed optical data are fundamental to be integrated into biogeochemical models, since the key role of the optical properties on lower trophic dynamics. In this paper, it is shown how ocean optics satellite products are used to constrain the optical algorithm adopted in the operational biogeochemical model system MedBFM that produces analyses, forecasts and reanalyses for the Mediterranean Sea biogeochemistry within the European Copernicus Marine Environment Monitoring Service (CMEMS).

Two different data sets of diffuse attenuation coefficients (K_d) for downward planar irradiance were used in MedBFM to carry out three 15-year simulations. The first simulation is based on climatological values retrieved with a global algorithm; the second uses an updated, interannually variable product from 4 different sensors, obtained with a regional algorithm specifically developed for the Mediterranean Sea; the third is forced by a climatological data set extracted from the updated algorithm. Differences between the two K_d data sets are evaluated in terms of the adopted/differing remote sensing algorithms, and the impact of the two different optical forcings on the MedBFM model output is quantified, with a specific focus on chlorophyll, also distinguishing the effect of using the interannually variable K_d by the one related to the algorithm upgrade.

The differences between the interannually variable K_d data set and the climatological one amount to 10%, resulting in local variations of chlorophyll vertical profile concentration, larger than 20% in some periods of the year. Noticeable effects are also observed on the along-basin zonal range of deep chlorophyll maximum depths during the simulated period, which increases with the use of the updated K_d data set. In the western Mediterranean, interannual variability of chlorophyll in summer grows up to 40% at 100 m.

Matching-up the updated model outputs with quality-controlled Biogeochemical-Argo floats data of fluorescence-derived chlorophyll results in a small increase of the model skill.

1. Introduction

In the recent decades, satellite sensors measuring ocean colour have been providing an ample global data set with a constant temporal acquisition frequency. Despite the major shortcomings (i.e., sensitivity to cloud coverage, limitation to euphotic depth) of satellite data, their use to validate biogeochemical models is profitable and well documented, as shown in Gregg et al. (2009), Doney et al. (2009), Dutkiewicz et al. (2015, 2019), and Salon et al. (2019), the latter for a brief review of Mediterranean Sea applications.

Combining numerical models and satellite products by means of data assimilation can additionally surpass limitations of separate techniques, and has been therefore widely accepted within the scientific community. The application of data assimilation schemes to satellite-estimated chlorophyll might positively impact the simulation of biogeochemical processes by improving multi-year state estimates (Simon

et al., 2015; Ciavatta et al., 2016, 2019; Fennel et al., 2019; Groom et al., 2019; Teruzzi et al., 2018, 2014b; Song et al., 2016a,b,c; Mattern et al., 2017) or by parameter optimization (Ciavatta et al., 2011).

Remote sensing can additionally supply information for the optical component settings embedded in biogeochemical models (Lazzari et al., 2012). Methods of light implementation in ecological and biogeochemical models range from simple exponential functions of photosynthetically available radiation (PAR), as done in Lazzari et al. (2010), to fully coupled radiative transfer models, as shown in Dutkiewicz et al. (2015). Simplified versions of optical models may adopt apparent optical properties estimated from satellites. Therefore, the choice of information retrieved from remote sensing becomes crucial for the correct representation of biogeochemical dynamics, expressed in terms of productivity and spatial and temporal distribution of biogeochemical variables, and may vary depending on the specific aspect to be

* Corresponding author.

E-mail address: eterzic@inogs.it (E. Terzić).

addressed. Nonetheless, efforts to use multi or hyperspectral models to integrate radiometry data with inherent and apparent optical properties, thus embedding the radiative transfer theory into biogeochemistry, have been recently implemented also in regional models (e.g. Skákala et al., 2020; Lazzari et al., 2020).

The scope of the present work is to evaluate how interannually variable apparent optical properties may affect the spatio-temporal variability of the Biogeochemical Flux Model (BFM; Vichi et al., 2007; Lazzari et al., 2012, 2016), which is the core of the MedBFM system, operational within the European Copernicus Marine Environment Monitoring Service (CMEMS). The analysis is focused on the impact of changing diffuse attenuation coefficients of downwelling irradiance (K_d) from single-sensor climatological (K_d^{ref}) to multi-sensor interannually variable (K_d^{new}) values, using data retrieved from CMEMS (based on ESA-CCI multi-sensor reflectance and including a regional algorithm, which should be more adequate for applications in the Mediterranean Sea). The primary goals are: firstly, to estimate how the new K_d data set changes the temporal and spatial variability of the biogeochemical dynamics, specifically in terms of the chlorophyll field and the deep chlorophyll maximum (DCM) feature; and secondly, to evaluate the degree of improvement in the MedBFM model skill, focusing on the CMEMS chlorophyll product quality. The former was tackled by separating the effect of the sensor upgrade by the one related to the introduction of the interannual variability. The latter was carried out considering key chlorophyll metrics (Salon et al., 2019) by comparing model profiles with a quality-controlled Biogeochemical Argo (BGC-Argo) floats data set, previously described in Organelli et al. (2017) and also adopted by Terzić et al. (2019).

While a number of experimental analyses of the diffuse attenuation coefficient properties were already assessed (Morel and Maritorena, 2001; Morel et al., 2007a,b; Organelli et al., 2017), a study of such kind is, to the authors' knowledge, a first attempt to evaluate the impact of different diffuse attenuation products on a multi-year biogeochemical simulation. Section 2 describes the methods employed in the paper, Sections 3 and 4 show the results and discuss them in terms of different effects observed in temporal and spatial variability, as well as for operational purposes concerning the quality of CMEMS chlorophyll products, and Section 5 draws the conclusions.

2. Methods

An integrated approach, based on a set of three numerical simulations carried out with the MedBFM model (1999–2015 period) and a recently delivered data set of biogeochemical Argo (BGC-Argo) floats observations, was used to assess how the new diffuse attenuation coefficient for downwelling irradiance may affect the 3-dimensional chlorophyll field (hereafter also referred to as Chl).

2.1. Biogeochemical model

The biogeochemical model BFM (Vichi et al., 2007, 2013) is a biomass-based numerical model that simulates biogeochemical fluxes of carbon, phosphorus, nitrogen, silicon, and oxygen, characterizing the lower trophic level (producers, consumers, and recyclers) of the marine ecosystem. The current version of BFM includes nine plankton functional types (PFTs): phytoplankton PFTs comprise diatoms, flagellates, picophytoplankton and dinoflagellates; heterotrophic PFTs contain carnivorous and omnivorous mesozooplankton, bacteria, heterotrophic nanoflagellates and microzooplankton. The non-living compartment is separated into three groups: labile, semi-labile and refractory organic matter. BFM is coupled also to a carbonate system model (Cossarini et al., 2015; Canu et al., 2015), which contains two prognostic state variables: alkalinity and dissolved inorganic carbon, and provides pH, partial pressure of CO_2 and air-sea CO_2 flux. In the MedBFM modelling system, which produces analyses, forecasts and reanalyses of the Mediterranean Sea biogeochemistry for CMEMS (see Salon et al., 2019,

for further details), BFM is coupled with the OGSTM transport model, featuring OGSTM-BFM (Lazzari et al., 2010, 2012, 2016; Cossarini et al., 2015), where OGSTM is based on the OPA 8.1 system (Foujols et al., 2000). MedBFM assimilates satellite-estimated chlorophyll concentration data through a variational scheme (Teruzzi et al., 2014b, 2018), and is offline driven by daily physical forcings (temperature, salinity, currents) provided by the NEMOV3.6 model within the CMEMS regional consortium for the Mediterranean Sea (Clementi et al., 2019).

In BFM, the phytoplankton photosynthesis and the chlorophyll-to-carbon ratio adaptation to different light regimes are regulated by PAR according to Geider's formulation (Geider et al., 1998). Surface PAR values are obtained from the ECMWF atmospheric model output (provided within the CMEMS regional consortium for the Mediterranean Sea), where the shortwave radiation Q_s (roughly between 0.2 and 4 μm) refers to radiation emitted by the Sun, then scattered, absorbed or transmitted by the atmosphere and reflected or absorbed by the surface (Hogan and Bozzo, 2018). Following Ebenhoh et al. (1997), PAR (i.e. the visible portion of Q_s) is then estimated with a multiplying factor of 0.5. The Beer–Lambert light model, used to evaluate the amount of irradiance available for photosynthesis at any vertical level of the MedBFM model, takes diffuse attenuation coefficients at 490 nm from satellites (K_{d490}):

$$PAR_d(z) = PAR_d(z_0)e^{-K_d(x,y,z,t)z} \quad (1)$$

where

$$K_d(x, y, z, t) = K_{d490}(x, y, t). \quad (2)$$

In the equations above, $PAR_d(z_0)$ is PAR at the surface level (z_0), $K_d(x, y, z, t)$ is equal to the diffuse attenuation coefficient at 490 nm from satellite, whereas x , y , z and t are longitude, latitude, depth and time respectively. Hereafter, $K_{d490}(x, y, t)$ is denoted as $K_d(490)$.

In the present work, we have adopted the MedBFM model with the meshgrid based on 1/16 degree longitudinal scale factor and on $1/16^\circ \cos(\phi)$ latitudinal scale factor (ϕ is the latitude). The vertical meshgrid accounts for 72 vertical z-levels: 25 in the first 200 m depth, 31 between 200 and 2000 m, 16 below 2000 m. Model chlorophyll outputs have been produced at weekly frequency. Further details on the simulations carried out are in Section 2.5.

2.2. BGC-Argo float data set

Fluorescence-derived chlorophyll data along the water column were utilized from the BGC-Argo float network (see Organelli et al., 2016 and Terzić et al., 2019). A total of 31 floats were acquired for the period between 2012 and 2016 for the Mediterranean basin, with 1314 vertical profiles of Chl concentration (units of mg m^{-3}) derived from fluorescence. Data acquisition had nominally a 10 m vertical resolution between 250 and 1000 m, 1 m from 10 to 250 m, increasing to 0.20 m from 10 m to the surface (Organelli et al., 2016). Each cast started from 1000 m parking depth at an adequate time in order to reach the surface around local noon (with a time window of two hours). BGC-Argo data employed in the present work have been used after quality control procedure, which includes the non-photochemical quenching correction (Xing et al., 2018; Bittig et al., 2019).

According to the Mediterranean Sea partition also used in CMEMS (Salon et al., 2019), the profiles were available for 13 out of 16 sub-basins (Fig. 1), with the majority in the north western Mediterranean (NWM, 332), followed by northern Ionian (ION3, 170) and southern Tyrrhenian (TYR2, 162). Data were not present in the western Ionian (ION1), northern Tyrrhenian (TYR1) and the eastern Levantine (LEV4); 7 profiles were collected in the northern Adriatic (ADR1) and only one in the western Levantine (LEV1).

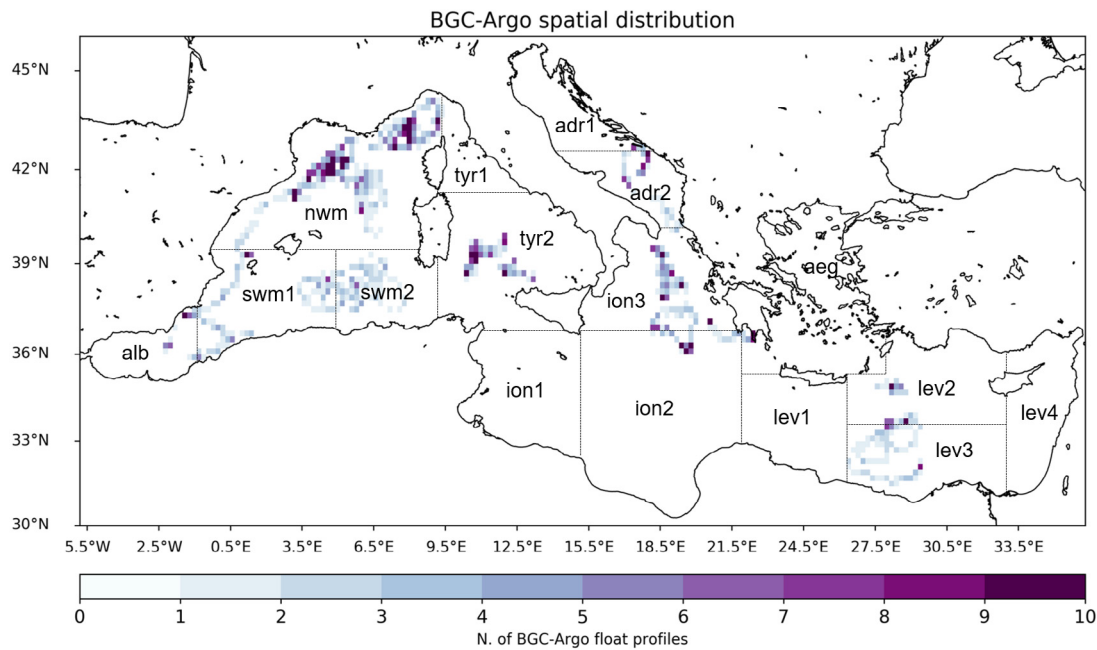


Fig. 1. Spatial distribution of chlorophyll vertical profiles measured by BGC-Argo floats superimposed to the sub-basin partition used in the Mediterranean CMEMS regional system. Sub-basins (with abbreviations) are: Aegean Sea (AEG), Alboran Sea (ALB), southwestern Mediterranean west (SWM1), southwestern Mediterranean east (SWM2), northwestern Mediterranean (NWM), northern Tyrrhenian Sea (TYR1), southern Tyrrhenian Sea (TYR2), western Ionian Sea (ION1), eastern Ionian Sea (ION2), northern Ionian Sea (ION3), northern Adriatic Sea (ADR1), southern Adriatic Sea (ADR2), western Levantine Sea (LEV1), northern Levantine Sea (LEV2), southern Levantine Sea (LEV3), eastern Levantine Sea (LEV4). The total number of BGC-Argo float profiles is reported in parentheses.

2.3. K_d data sets

Two $K_d(490)$ data sets are integrated in the MedBFM model. The first one (hereafter K_d^{ref}) consists of a bi-weekly climatology derived by the SeaWiFS data (Sea-Viewing Wide Field-of-View Sensor, years 1998–2004, see Lazzari et al., 2012). The second data set (hereafter K_d^{new}) is interannually variable with a weekly frequency, covers the period 1998–2015, and was computed for CMEMS merging SeaWiFS, MODIS-Aqua, MERIS, and VIIRS sensors (for more details see Volpe et al., 2019).

While K_d^{ref} is derived by a global algorithm, the K_d^{new} time series have been computed by a specifically developed and tuned algorithm for the Mediterranean Sea (Volpe et al., 2017), therefore it is henceforth referred as CMEMS multi-sensor regional product (REP-CMEMS). Note that we retrieved the REP-CMEMS product in 2018 as v01 version based on ESA-CCI reflectance (Volpe et al., 2017). Both data sets have been spatially interpolated from their original 1 km resolution on the model grid at 1/16 degree.

The K_d^{ref} tuning procedure adopted in Lazzari et al. (2012) was based on a series of simulations to compare the model output with in-situ values of DCM depth and magnitudes during summer in the Levantine basin (data from Turley et al., 2000, and Moutin and Raimbault, 2002), resulting in a multiplication factor of 1.2 of the original $K_d(490)$ values. The tuning procedure was included in the model simulations due to the uncertainty related to the use of mono-spectral values of $K_d(490)$, while the DCM depth is the cumulative biogeochemical effect resulting from the interaction of the entire light spectrum (represented by PAR) with phytoplankton (Cullen, 2015; Mignot et al., 2014; Terzić et al., 2019).

Similarly, after a comparison with the tuned K_d^{ref} values for the same season and sub-basin, K_d^{new} resulted in a multiplication factor of 1.3. The little difference between the tuning factors is due to the two algorithms adopted to produce the data sets K_d^{ref} and K_d^{new} . More specifically, the algorithm used to compute diffuse attenuation coefficients of downwelling irradiance at 490 nm for the CMEMS multi-sensors product is a fourth power polynomial expression of the remote sensing reflectance ($R_{rs}(\lambda)$) ratio ($R_{rs}(490)$ to $R_{rs}(555)$), denoted as

Table 1

Coefficients used to retrieve the original data set of $K_d(490)$. For K_d^{ref} (O'Reilly et al., 2000), the global algorithm for SeaWiFS is applied with a tuning factor (T.F.) of 1.2. For K_d^{new} , the regional MedKd is used instead, with coefficients reported in Volpe et al. (2017), and a tuning factor (T.F.) of 1.3.

Algorithm	Model	a_0	a_1	a_2	a_3	a_4	T.F.
SeaWiFS	K_d^{ref}	-0.8515	-1.8263	1.8714	-2.4414	-1.069	1.2
MedKd	K_d^{new}	-0.7713	-2.2864	3.6408	2.3152	-5.172	1.3

$\rho_{490/555}$, and shown in Eq. (3), whereas the $K_d(490)$ calculation is written in Eq. (4):

$$\rho_{490/555} = R_{rs}(490)/R_{rs}(555) \quad (3)$$

$$K_d(490) = K_w(490) + K_{bio}(490) \quad (4)$$

where $K_w = 0.0166$ and $K_{bio} = 10 \sum_{n=0}^4 a_n (\log_{10} \rho_{490/555})^n$ are the diffuse attenuation coefficients of the pure water and biogenic components respectively. Note that the regional algorithm for the Mediterranean Sea as reported in Volpe et al. (2017), successively named “MedKd” in Volpe et al. (2019), differs from the global (see Table 1), and therefore also the algorithm for the climatological data set (K_d^{ref}) differs from the interannually variable one (K_d^{new}).

The MedBFM model needs $K_d(490)$ maps that fully cover the Mediterranean basin surface. Daily data of K_d^{new} provided in the CMEMS catalogue¹ were used to calculate weekly averages at the model resolution of 1/16°. The maps resulting from the temporal average and the spatial interpolation are still affected by cloud coverage. Gaps in the K_d maps have been filled with a two-step replacement strategy using monthly averaged maps and a climatology both built using the K_d^{new} time series. Firstly, missing values in each weekly map are replaced with the monthly mean of the corresponding month. Then, in case

¹ The product OCEANCOLOUR_MED_OPTICS_L3_REP_OBSERVATIONS_009_095 is continuously updated as reported in the CMEMS catalogue: the most recent version is documented and validated in Colella et al. (2021).

of still incomplete coverage, gaps are replaced in a second step with the climatological values. Since the relatively high coverage of the weekly average (>80% at basin scale) and of the monthly average (>95%), the effects of spatial discontinuities potentially introduced by the replacement procedure can be considered marginal with respect to the spatial and temporal scales of the analysis carried out in the present work.

2.4. K_d data set differences

Climatological monthly maps of K_d^{new} data set are shown in Fig. 2. Highest values (0.10 m^{-1} or higher) are displayed during late autumn, winter and early spring months, especially in the western basin. The peak is between March and April in the northwestern Mediterranean, which might coincide with the late winter/early spring bloom period. Constantly higher values are noticed also for the northern Aegean and Alboran seas. In this respect, it is worth mentioning that, from the modelling side, these regions may present large uncertainties due to insufficiently accurate boundary conditions (i.e. connecting the Mediterranean Sea with the Black Sea in the former and with the Atlantic Ocean in the latter case, see for example Salon et al., 2019) and are thus less emphasized in following elaborations. Lowest values (around 0.03 m^{-1}) are observed in the Ionian and Levantine sub-basins almost throughout the entire year, with increasing values between December and February (reaching 0.06 m^{-1}). A clear east–west gradient can be observed, with values increasing westward.

Climatological monthly maps of differences ($K_d^{new} - K_d^{ref}$) normalized with K_d^{ref} values demonstrate how the spatial variability of satellite-derived K_d is affected by the use of the REP-CMEMS data set (Fig. 3). Major discrepancies are seen for the western sub-basins in the late winter/early spring period, where bi-weekly climatological K_d^{new} values are up to 10% different compared to K_d^{ref} . REP-CMEMS values are almost overall lower than SeaWiFS in August and September, whereas slight fluctuations of K_d values are observed during autumn and early winter, the last period characterized by a positive difference in the Tyrrhenian Sea. Because of the tuning procedure, the sum of the differences over June, July and August in the Levantine basin is negligible.

2.5. Simulations protocol

The MedBFM model was run to simulate the Mediterranean Sea biogeochemistry for the period between 1999 and 2015, using the two different diffuse attenuation coefficient data sets $K_d(490)$ described in Section 2.3: K_d^{new} and K_d^{ref} . We carried out three simulations (Table 2), namely, S^{ref} (forced with K_d^{ref}), S^{new} (forced with interannually variable K_d^{new}), and $S^{new(clim)}$ (forced with a climatology computed from K_d^{new} , at the same bi-weekly temporal frequency of K_d^{ref}). The $S^{new(clim)}$ simulation is critical to evaluate the impact of the new sensor and algorithm (comparing the simulations forced by the REP-CMEMS and the SeaWiFS climatological data sets, i.e. $S^{new(clim)}$ vs. S^{ref}) and the impact of introducing an interannually variable K_d (comparing the simulations forced by the variable and climatological data sets, i.e. S^{new} vs. $S^{new(clim)}$). The reference simulation S^{ref} is available in the CMEMS catalogue² and its quality has been already described in Teruzzi et al. (2014a). Here we focus on the anomalies among the three model configurations that differ only in terms of the diffuse attenuation coefficients adopted.

Our analysis was constrained only to open ocean areas, i.e. deeper than 200 m (as already done in Lazzari et al., 2012, 2016), leaving the interpretation of coastal regions for future computations with a more sophisticated light model.

Table 2

Summary of the simulations with corresponding details of forcing K_d data set.

Simulation	K_d data set	K_d temporal frequency
S^{ref}	K_d^{ref}	Climatological, bi-weekly (26 K_d maps, repeated every year)
$S^{new(clim)}$	K_d^{new}	Climatological, bi-weekly (26 K_d maps, repeated every year)
S^{new}	K_d^{new}	Interannually variable, weekly (52 K_d maps, changing every year)

3. Results

In this section we assess how the interannually variable K_d^{new} , produced through the regional algorithm from 4 different sensors (and retrieved from the CMEMS catalogue), affects (1) the chlorophyll horizontal and vertical distributions, and its temporal variability, and (2) the quality of the corresponding CMEMS product.

3.1. Impact of K_d^{new} on the chlorophyll field

Model outputs for both simulations are evaluated in terms of Chl concentrations (units of mg m^{-3}); anomalies are calculated as the differences between $S^{new(clim)}$ and S^{ref} simulations, normalized with values from S^{ref} , and between S^{new} and $S^{new(clim)}$ simulations, normalized with values from $S^{new(clim)}$. Chl values at surface, 50 m and 100 m along the seasonal cycle are shown for March, June, September and December.

At surface (Fig. 4), highest Chl concentrations are observed in March for the western basin (larger than 0.5 mg m^{-3} in the northwestern Mediterranean), while the rest of the basin displays oligotrophic values (lower than 0.2 mg m^{-3}), which holds true for all regions in June and September, with values increasing again in December in the western Mediterranean (0.3 mg m^{-3}). The second column of Fig. 4 depicts the normalized difference between S^{new} and $S^{new(clim)}$, showing that the impact of the interannual variability related to the REP-CMEMS data set is spatially distributed with a certain patchiness, with the main effect of increasing the Chl concentration of few percents (e.g., maximum of 7%) in the western Mediterranean and southern Adriatic Sea during March. In March, over the rest of the basin, and in December we observe a slight decrease of surface Chl, while the effect in the warm semester seems quite negligible. The change from SeaWiFS to REP-CMEMS data set (right column of Fig. 4) shows comparable positive variations in the Tyrrhenian Sea in March and December, in the latter also near the Atlantic inflow and along the eastern coasts. As expected, the effect of upgrading the climatology is more uniformly distributed than what observed by introducing the interannual variability, with a tendency to affect more the coastal areas (see in March along the Liguro-Provencal coast, the Tyrrhenian coast, the south-eastern Levantine coast, the latter more intense in December). A close-up on March in the western Mediterranean (Fig. 3) reveals an increase in K_d values in the southern regions and a decrease north. The resulting surface Chl values in turn exhibit a more substantial decrease over the northern sector when comparing the simulation forced by the bi-weekly REP-CMEMS climatology with the one driven by SeaWiFS, and an increase due to the interannually variable K_d , meaning that in this area the change of sensor and algorithm is somehow counterbalanced by the increased variability related to the REP-CMEMS data set.

At 50 m (Fig. 5), the impacts of the K_d upgrades are larger than what was observed at surface, in particular in March in western sub-basins but with positive differences also in June in the Levantine and in December in the south-western areas, although with lower values of chlorophyll. In March, the change from SeaWiFS to REP-CMEMS data set shows a K_d decrease (increase) in the north-western (south-western) areas (and also in the western Tyrrhenian and northern Ionian Seas, Fig. 3), meaning an increase (decrease) of water transparency, and

² MEDSEA_REANALYSIS_BIO_006_008.

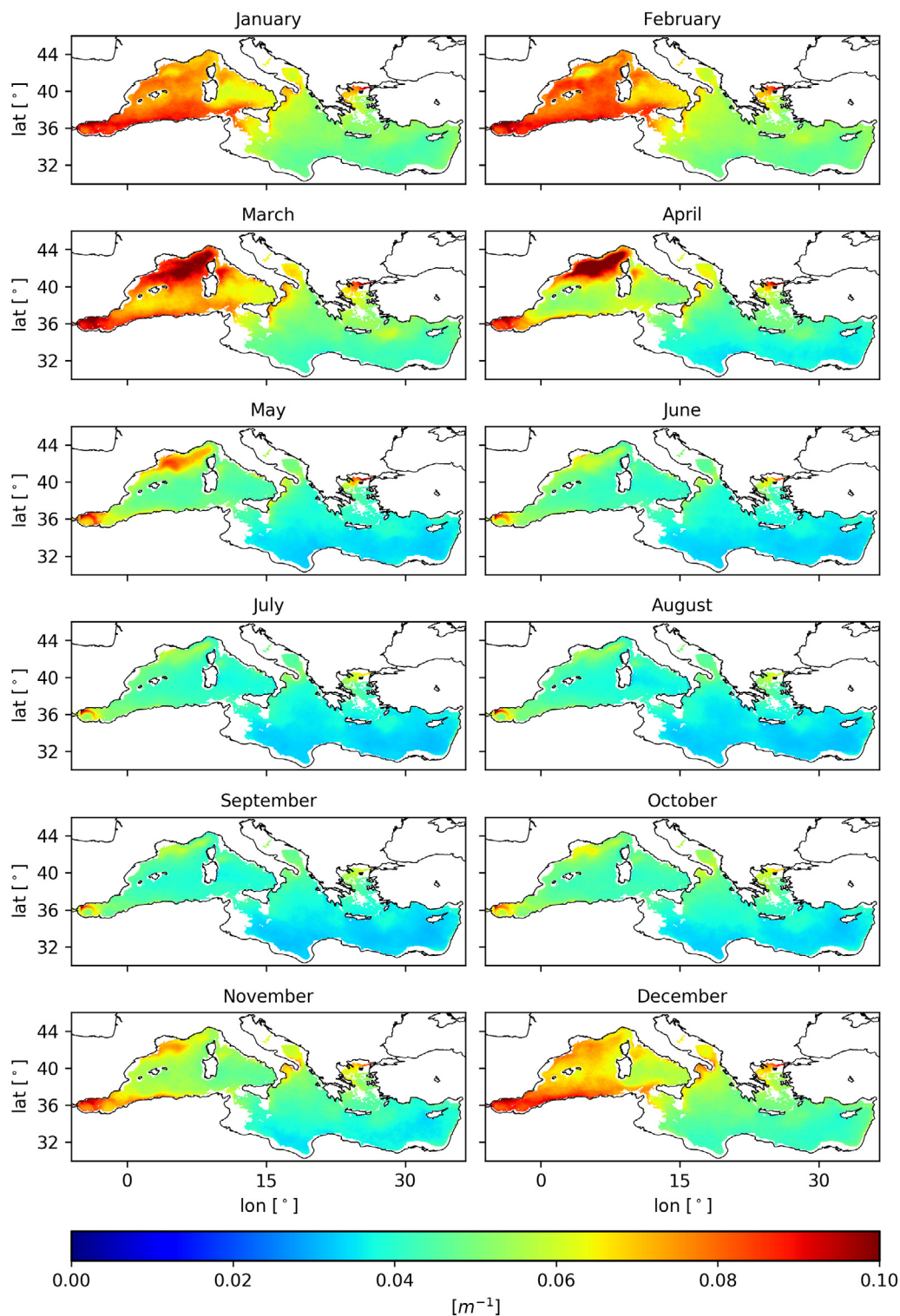


Fig. 2. Climatological monthly mean maps of the interannually variable K_d^{new} , units of m^{-1} . Data from CMEMS (see text for details).

therefore an increase (decrease) of Chl concentration during the late winter bloom, comparing $S^{new(clim)}$ with S^{ref} simulations (right column of Fig. 5). On the other side, the interannually variable K_d tends to uniformly increase Chl concentration over the whole western Mediterranean, further increasing Chl concentration in the most productive area of the Gulf of Lions, and partially reducing the effect over the south-western areas. The 50 m layer could be representative of typical DCM depths in western sub-basins (Boldrin et al., 2002) with enhanced values persisting until September, consistently to the DCM dynamics in

the west, emerging between May and October (Lavigne et al., 2015). In the period of DCM (June and September in Fig. 5), we observe that increases (decreases) of K_d^{new} compared to K_d^{ref} (Fig. 3) roughly correspond to increase (decrease) of Chl concentrations in the S^{new} simulation, showing a decoupling of the chlorophyll vertical structure between the surface and the DCM level. The impacts observed in S^{new} appear much lower during this period.

Maximum Chl concentrations at 100 m depth (Fig. 6) are present in June and September in the central-western and eastern basin (0.4

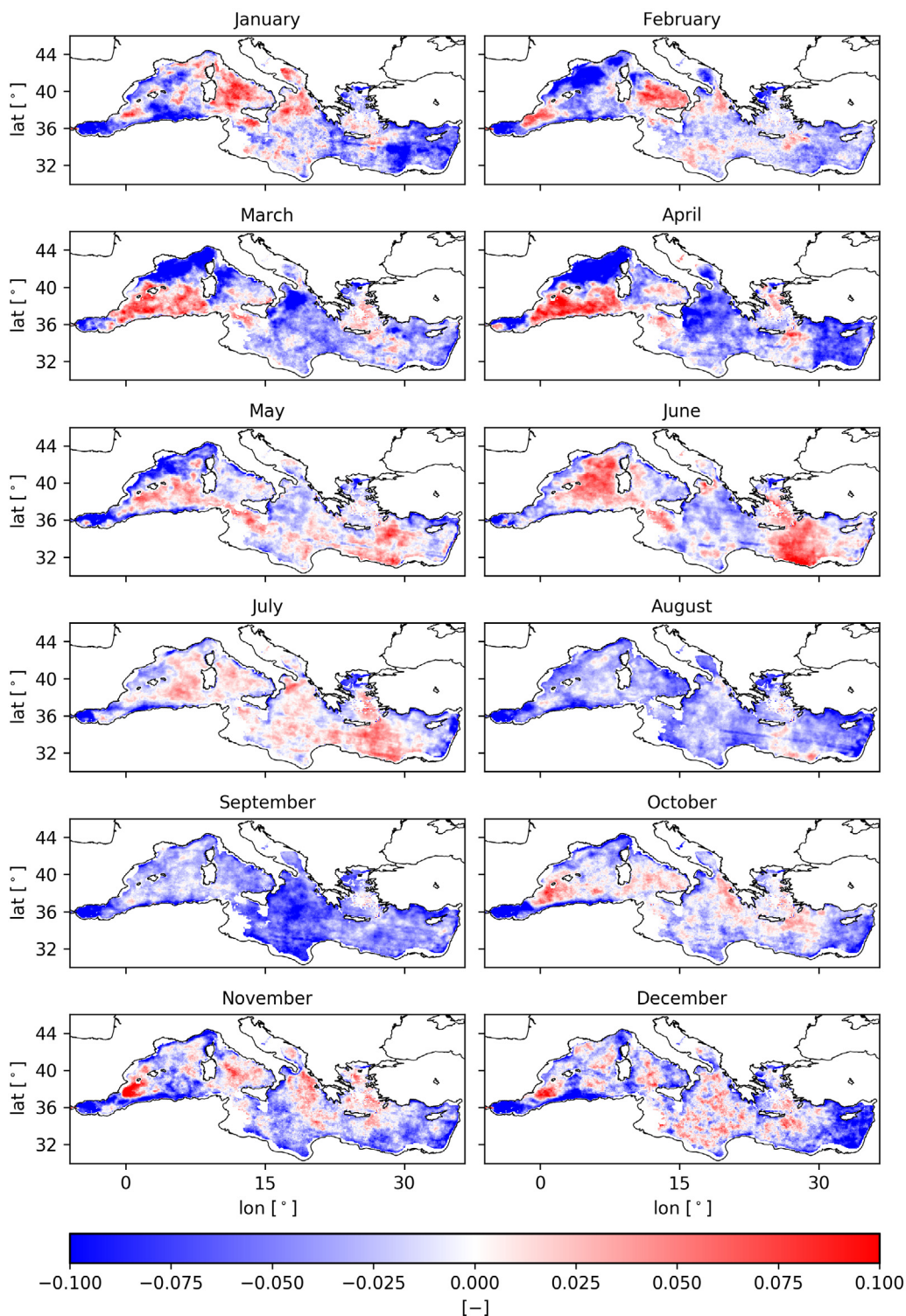


Fig. 3. Climatological monthly mean maps of the difference between K_d^{new} and K_d^{ref} , normalized with K_d^{ref} .

mg m^{-3}) in agreement with the DCM depth late spring formation and stabilization throughout the summer and autumn months, i.e. from April to November. The variations in S^{new} with respect to $S^{new(clim)}$ observed at 100 m in the north-western sub-basin in June are larger than 100% (also due to decreasing values of chlorophyll at this depth), possibly explained with a shift in DCM depth. The effect of upgrading from SeaWiFS to REP-CMEMS is also more intense in September, with

a general increase in Chl concentration mainly located in the western basin and Adriatic and Aegean marginal seas. The coastal areas, specifically in the Tyrrhenian Sea, are affected in June.

The DCM is an ubiquitous feature of the chlorophyll vertical profile dynamics in oligotrophic environments and between late spring and autumn in the Mediterranean Sea (Siokou-Frangou et al., 2010), displaying a zonal deepening from west to east, as well as meridionally from north to south (see Lazzari et al., 2012; Lavigne et al., 2015).

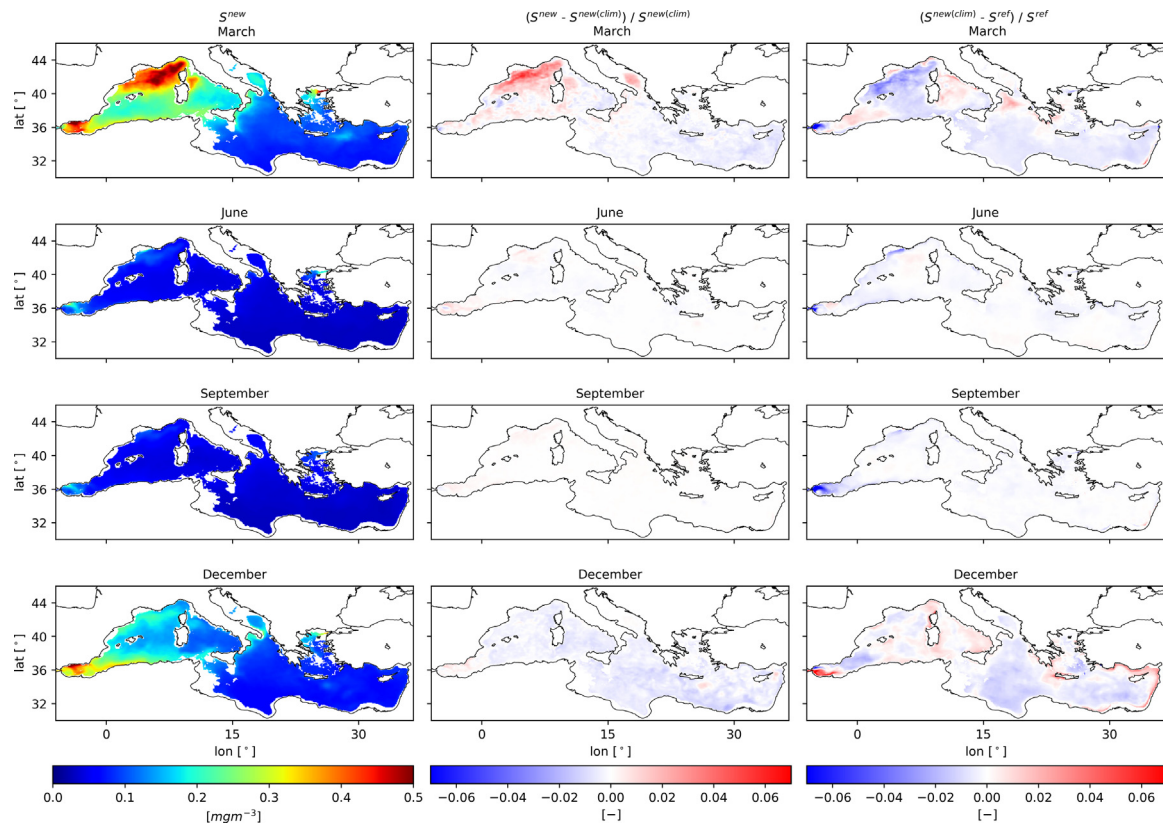


Fig. 4. Surface Chl output for March, June, September and December. Left column: results from S^{new} (units of mgm^{-3}); central column: difference between S^{new} and $S^{new(clim)}$, normalized with $S^{new(clim)}$, right column: difference between $S^{new(clim)}$ and S^{ref} , normalized with S^{ref} (unitless).

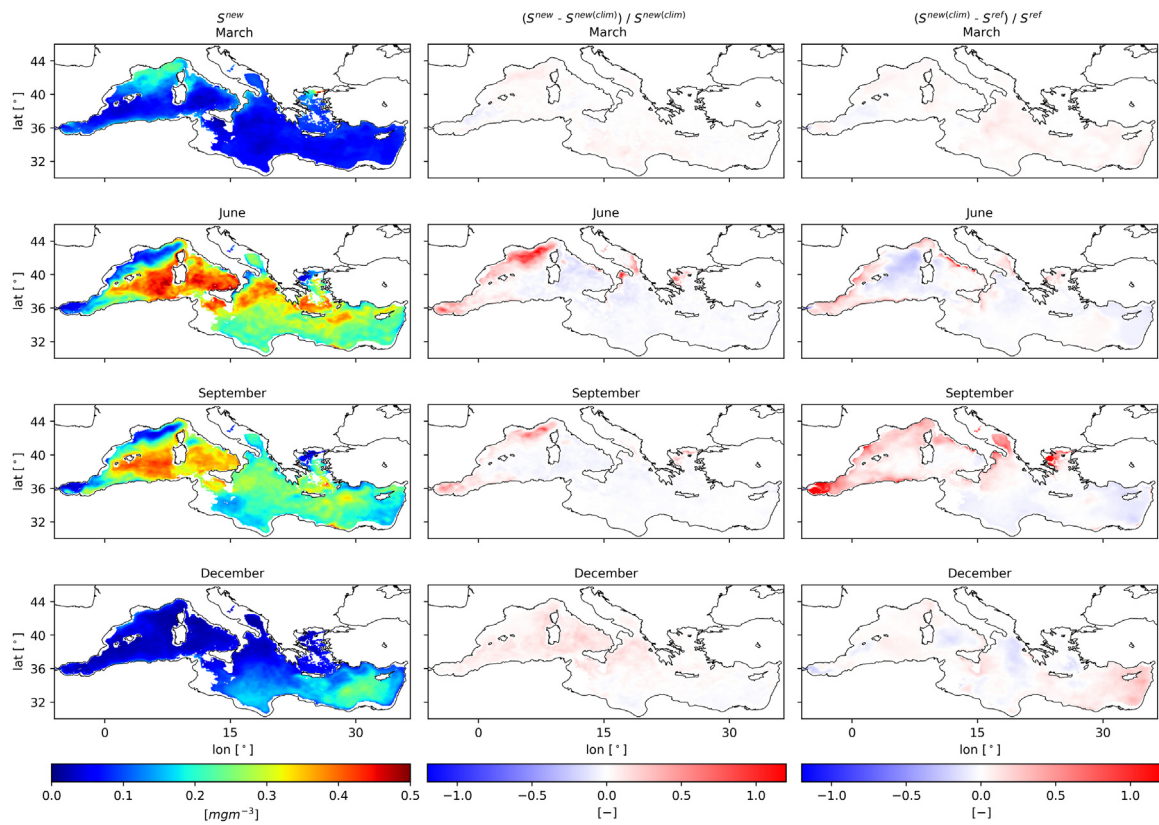


Fig. 5. As in Fig. 4 but at 50 m.

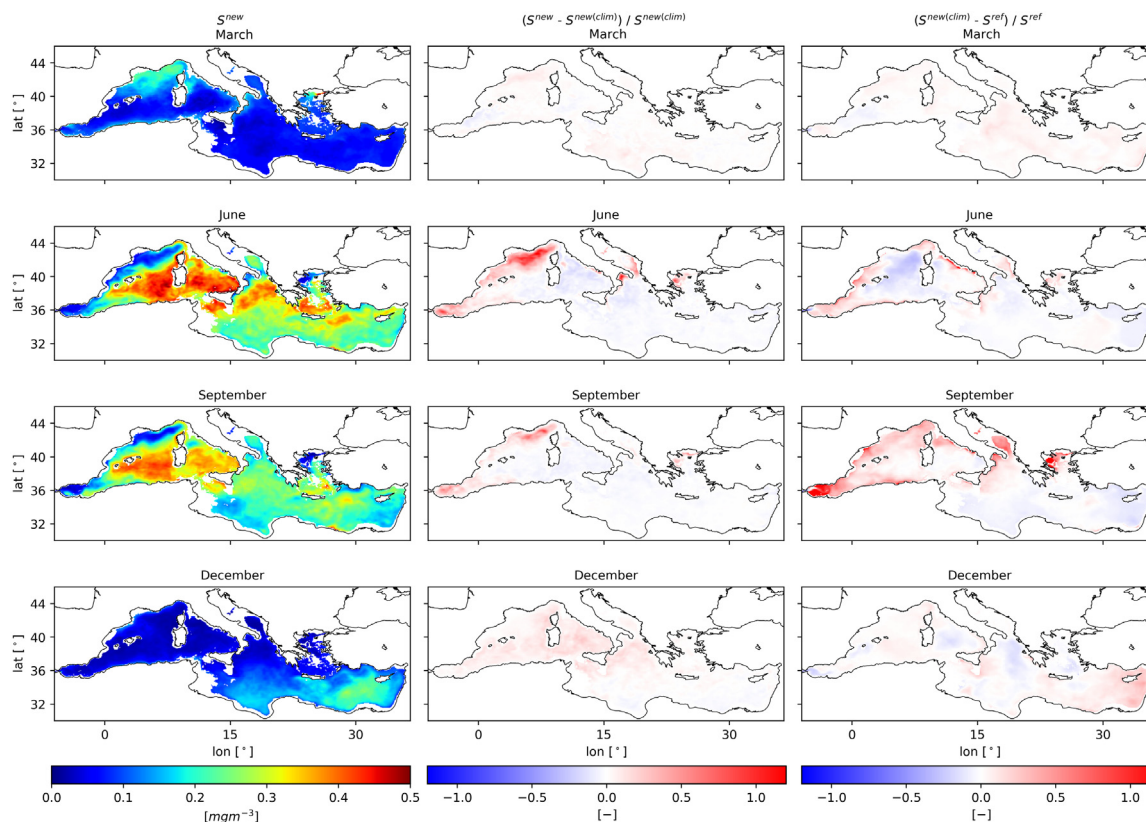


Fig. 6. As in Fig. 4 but at 100 m.

Oligotrophic environments, such as the eastern Mediterranean, are characterized by deep DCM and nitracline, which are concomitantly associated with lower Chl concentrations and primary productivity (Estrada et al., 1993), contrary to the areas with higher biological activity (such as the Ligurian Sea), which display shallower DCM with higher values of Chl.

The calculation of the DCM depth is based on the following criteria (see also Lavigne et al., 2015; Salon et al., 2019):

- depth of DCM should be deeper than 40 m and shallower than 200 m;
- Chl concentration at DCM depth should exceed 0.1 mg m^{-3} .

Monthly mean and standard deviation values of DCM depth, calculated for the S^{new} (respectively, $\overline{M^{new}}$ and $\sigma(M^{new})$ as defined in Appendix A, where M is the DCM depth and $\sigma(M^{new})$ is an indicator of the interannual variability), are shown in Fig. 7 (top) as coloured squares per each sub-basin (x-axis) and month (y-axis). The model confirms the presence of the DCM zonal gradient (Lavigne et al., 2015; Terzić et al., 2019), as well as the disappearance of the feature during winter months due to an enhanced convective mixing which destabilizes the water column. DCM depths in the Levantine range from 80 to 100 m in spring to up to 120 m in summer months (in agreement with Lavigne et al., 2015), with corresponding mean Chl concentrations between 0.2 and 0.3 mg m^{-3} (not shown), consistently with results shown in Christaki et al. (2001) and Dolan et al. (2002). In western basins, DCM depth ranges from 60 m in spring and autumn, increasing to 70–80 m in summer (in good accordance with Lavigne et al., 2015), with corresponding Chl values higher than 0.4 mg m^{-3} during summer and decreasing in autumn to 0.3 mg m^{-3} , mostly in NWM and Tyrrhenian Sea. The interannual variability of DCM depth in S^{new} (Fig. 7b) is between 4 and 8 m during the summer months, increasing to around 12 m in May, and reaching 14 m in the northern Adriatic and northern Ionian Seas.

The difference in DCM depth mean and standard deviation between the three simulations is shown in the middle and bottom rows of Fig. 7. On average, compared with S^{ref} , the DCM depth increases around 5 m with the updated diffuse attenuation coefficient: major differences in DCM depth arise in the Ionian sub-basins in May/June and September/October, with an increase in the mean larger than 8 m and in the standard deviation of up to 6 m (Fig. 7c). A DCM depth increase larger than 6 m is also observable in the eastern Levantine (LEV4). The general increase of the DCM depth during spring is specifically due to the effect of the interannually variable diffuse attenuation coefficient (Fig. 7e), while it rather tends to reduce DCM depth in October/November, with the result that the sensor upgrade plays an important role in increasing the DCM depth in this period more than the use of the interannually variable K_d^{new} .

The increase of the standard deviation in the DCM depth (Fig. 7d) quantifies the extension of the interannual variability simulated by S^{new} , demonstrating the role played by the updated, interannually variable K_d^{new} . As expected, we can observe from Fig. 7f that the increase of variability is almost totally referred to the use of the interannually variable K_d^{new} rather than its bi-weekly climatology.

The increased interannual variability of the DCM depth in S^{new} in the four months characterized by the presence of DCM in all the Mediterranean Sea (June to September, see Fig. 7) is also illustrated in Fig. 8, which displays a widening of the range of values covered by the DCM mean depth along the zonal direction estimated about 80%, i.e. from 7.9 to 14.4 m (while the sensor upgrade has a minor contribute, from 7.9 to 8.1 m). Considering the sub-basin averages in the same period, Fig. 9 confirms that, with K_d^{new} , the DCM depth deepens in most sub-basins between 2% and 5% in comparison with the reference (as also shown by the extension of the light red area in Fig. 8).

The increase of the DCM mean depth in S^{new} is coherent with an increase of the total chlorophyll biomass per area between 0 and 200 m in the period June–September, which results to be generally higher

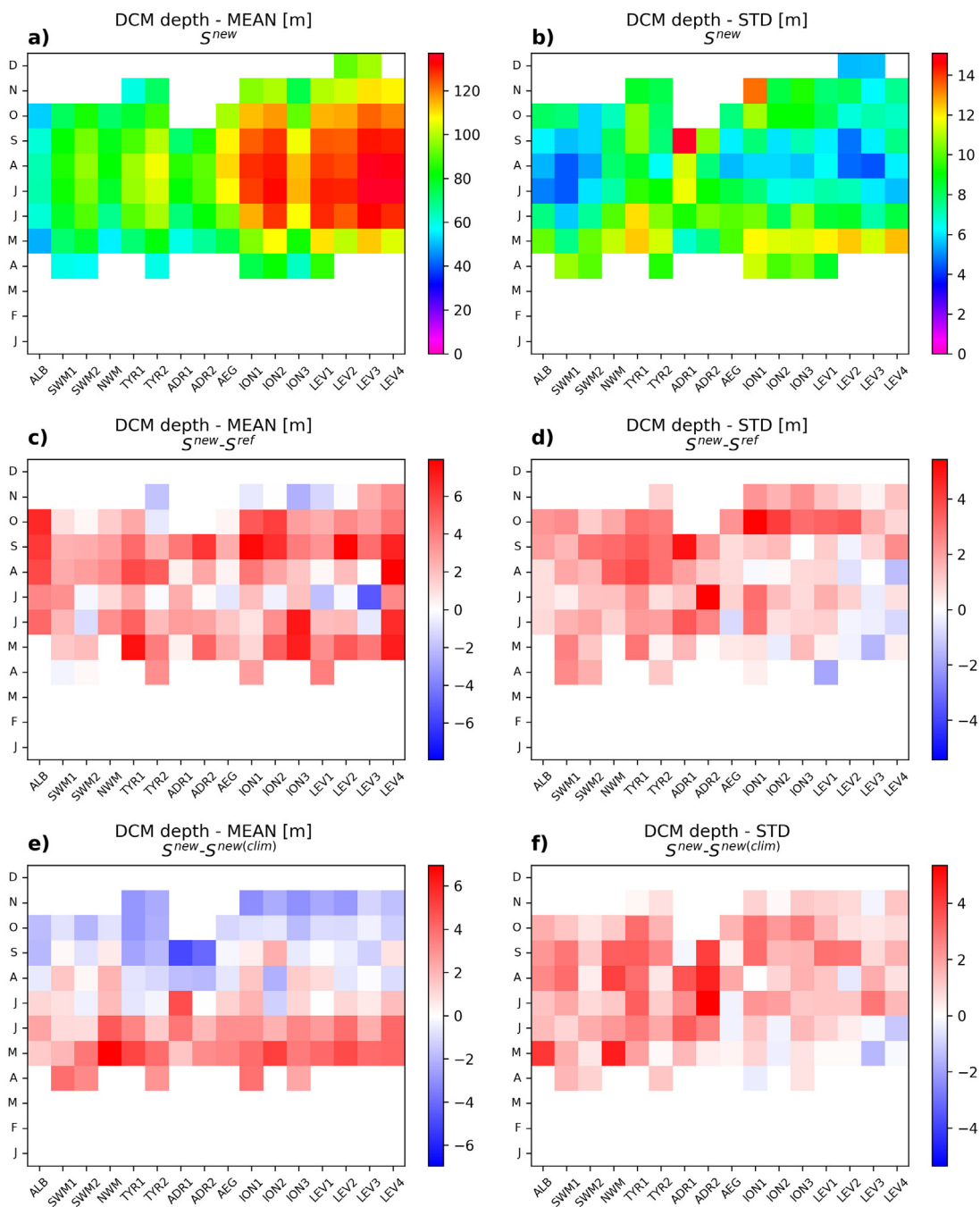


Fig. 7. Top row: DCM depth monthly mean, for each sub-basin and month (a) and standard deviation, for each sub-basin and month (b), calculated from S^{new} . Middle row: difference between S^{new} and S^{ref} DCM depth monthly means, for each sub-basin and month (c) and standard deviation, for each sub-basin and month (d). Bottom row: as middle row but between S^{new} and $S^{new(clim)}$.

than the reference simulation (up to 10% in the Alboran Sea). Such behaviour can be associated to the decreasing of the K_d^{new} between August and September (Fig. 3) and the observed deepening of the DCM which may allow a larger availability of nutrients to increase the chlorophyll biomass. However, a cautionary behaviour must be maintained to directly relate these evidences, since the DCM dynamics certainly involves optical properties related to light penetration, but also nutrient availability may play a role (Lavigne et al., 2015; Cullen, 2015), contrarily to physical processes of transport and mixing that are the same in the two simulations. Still, Fig. 8 shows a slight but positive increase in the range of values of total chlorophyll biomass per area in the 0–200 m layer along the zonal direction in the period

June to September (around 3%, i.e. from 3.9 mg m^{-2} to 4.01 mg m^{-2} , with 2% related to the sensor upgrade), demonstrating a limited but still extended interannual variability due to the introduction of K_d^{new} . Similar results are obtained considering the meridional mean of the 95th percentile of total chlorophyll biomass per area (not shown).

The difference in Chl values at DCM between S^{new} and S^{ref} (not shown) does not convey a uniform pattern, with a general decrease within the order of 10% and an increase of the same order especially in the eastern ones in August and September (differences less than 0.03 mg m^{-3}). Most of the decrease is related to the introduction of the interannually variable K_d . Similarly to the mean DCM depth, the difference in the standard deviation of the mean Chl value at DCM (not

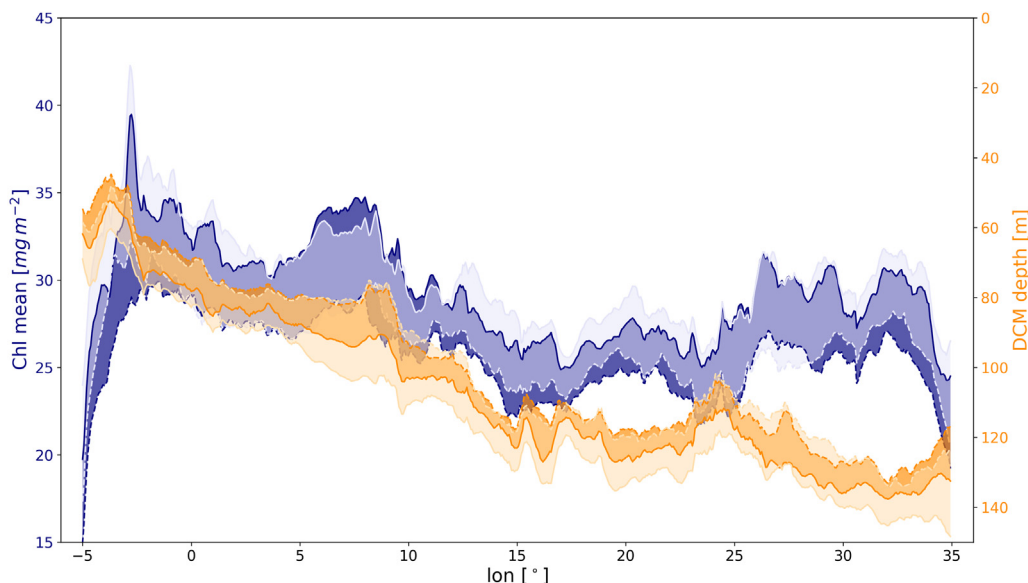


Fig. 8. Computation of the meridional mean of DCM depth (orange) and total chlorophyll biomass per area between 0 and 200 m (blue) for S^{ref} (dark orange/blue) and S^{new} (light orange/blue), during the period June–September. The distance between lower and higher orange (blue) thick line represents the range between minimum (dashed) and maximum (solid) values of DCM depth (total chlorophyll biomass per area) for each longitude. The mean range of DCM depth (total chlorophyll biomass per area) in S^{ref} is 7.9 m (3.90 mg m^{-2}), increasing to 14.4 m (4.01 mg m^{-2}) in S^{new} .

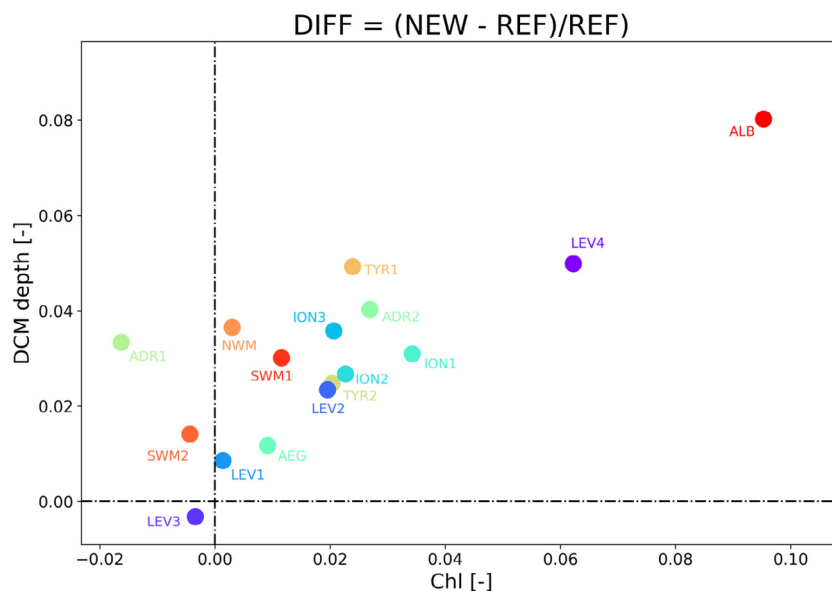


Fig. 9. Sub-basin averaged differences between S^{new} and S^{ref} , normalized with S^{ref} , of total chlorophyll biomass per area between 0 and 200 m (x-axis) and mean DCM depth (y-axis), during the period June–September.

shown) is overall positive, and almost totally due to the interannual variability introduced in S^{new} , revealing that the use of the updated K_d^{new} increases the range of Chl values at DCM, with larger differences during spring months at west, and highest values in the Adriatic Sea.

Further investigations to quantify the impact of the updated K_d coefficient on spatial and temporal scales confirm that the main effect of the interannually variable K_d in the upper 100 m is to extend both the spatial and interannual variability of the chlorophyll field between early spring and early autumn, with a maximum effect (about +40%) in the western sub-basins at 100 m during summer. More details are reported in Appendix A.

3.2. Impact of K_d^{new} on the model skill

The quality-controlled data set of bio-optical variables from BGC-Argo floats described in Section 2.2 has been used for the quality assessment of the chlorophyll variable. A point-by-point match-up was carried out between model chlorophyll output and BGC-Argo fluorescence-derived Chl data, which was followed by a spatio-temporal division (monthly values for 16 sub-basins). The model skill, in terms of chlorophyll product quality, was evaluated with three statistical parameters: Bias, root mean square error (RMSE) and the Pearson correlation coefficient (ρ), all reported in Appendix B.

The quality statistical parameters for the three simulations are summarized in Fig. 10. Fig. 10a, d and g show that negative Biases are

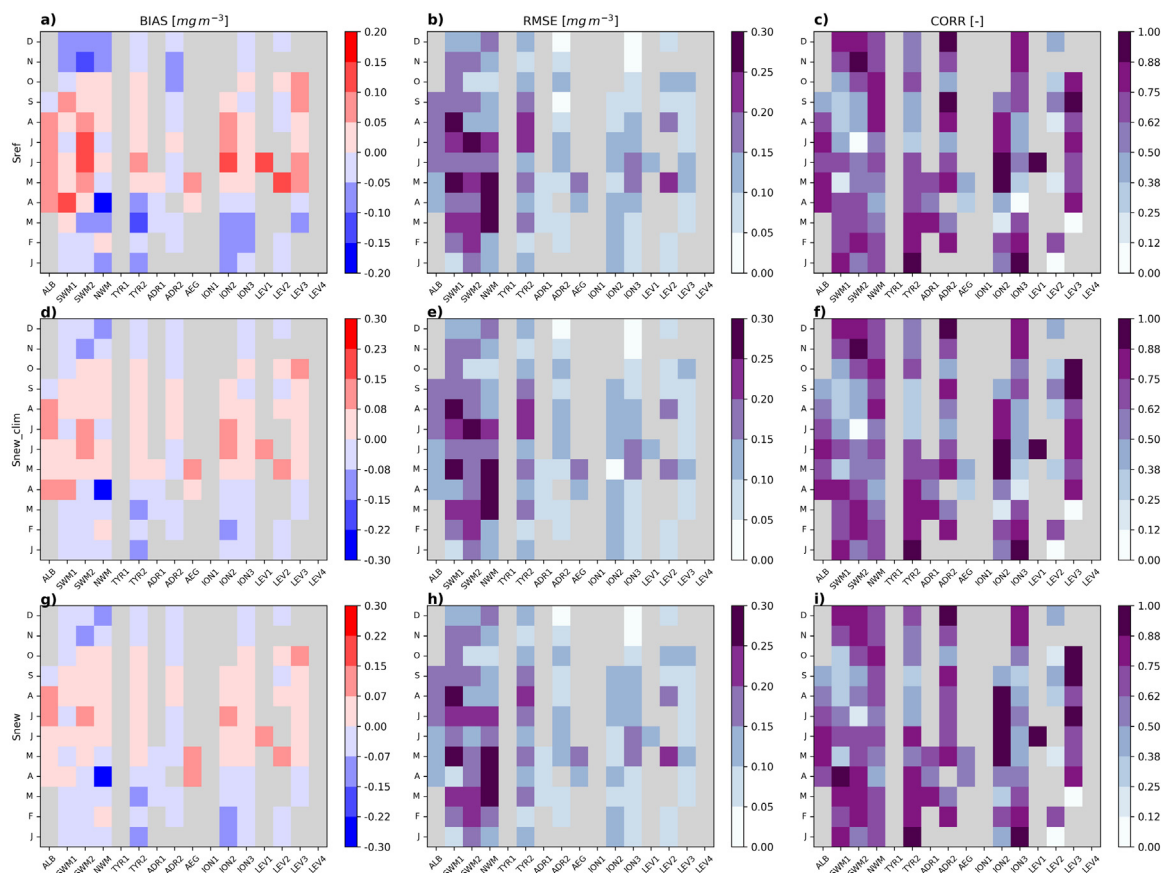


Fig. 10. Match-up between model chlorophyll outputs and available BGC-Argo floats data, expressed as Bias (a, d, g), RMSE (b, e, h) and correlation coefficient (c, f, i), for each sub-basin and month. Top row: S^{ref} , middle row: $S^{new(clim)}$, bottom row: S^{new} . Grey boxes indicate absence of BGC-Argo data.

present in winter and autumn, indicating that in the cold semester the model generally underestimates Chl for all regions, especially during spring in the northwestern Mediterranean (negative Bias of almost 0.3 mg m^{-3}). Similarly, Fig. 10b, e, h show that RMSE ranges between 0.1 and 0.2 mg m^{-3} for eastern and from 0.2 to 0.3 mg m^{-3} for western sub-basins (with an anomalous value of 1.1 mg m^{-3} in April in the northwestern Mediterranean due to values from BGC-Argo floats of up to 5 mg m^{-3} — not shown). Correlation coefficients (Fig. 10c, f, i) basically span from 0.2 in winter over the Levantine and 0.3 in autumn in the south-western sub-basins to 0.9 in the northern Ionian Sea between May and August. The values of the quality parameters are generally in line with the outcomes from the CMEMS analysis and forecast product (Bolzon et al., 2019).

Clear Bias differences between S^{new} and S^{ref} are mainly observed in spring: decrements in the Alboran Sea, southwestern Mediterranean, Ionian and Levantine areas show an improvement of the quality for the simulation implementing K_d^{new} , while $S^{new(clim)}$ does not exhibit any appreciable variation. A small reduction of the underestimation during autumn and winter, especially in the western sub-basins, is also visible, mainly due to the sensor upgrade.

Differences in RMSE and correlation among the different sub-basins and months appear quite small. In order to provide a synthesis of the impact of the new interannually variable data set and the one of the sensor upgrade only, the metrics of Fig. 10 are averaged in the seasonal statistics of Table 3. Given the uneven distribution of the BGC-Argo floats among sub-basins (as shown in Fig. 1, western sub-basins have an availability of data larger than eastern ones, with NWM, SWM1 and SWM2 surpassing 500 profiles, constituting almost 40% of the total number of profiles in the Mediterranean Sea), the spatial averages are representative of the actual data coverage and the eventual extrapolation to the whole Mediterranean Sea should be taken with

caution. Then, concerning the temporal distribution, the total number of match-ups in each season is roughly larger than 20 000. The most important effect is the reduction of the Bias in spring, which in S^{new} amounts to 0.023 mg m^{-3} , and is reduced by 24% from S^{ref} , and only by 4% with the sensor upgrade. Similarly, in spring RMSE is reduced by 6% (roughly equally divided by the impact in sensor upgrade and the interannual variable K_d) and correlation increases by 9% (66% of this increment is due to the use of the interannual variable K_d). The other seasons have lower differences, with winter showing a small improvement and summer/autumn a slightly decreased performance. When the $S^{new(clim)}$ run shows a decrease in performance (i.e., summer Bias and RMSE), the interannual variability partly mitigates it, supporting the importance of the time-varying information.

4. Discussion

The upgraded diffuse attenuation coefficient K_d^{new} resulted in a two-fold different product: firstly, the interannual variability was introduced for the period 1999–2015, and secondly, the product merged observations from 4 different satellite sensors, thus implementing a modified remote sensing algorithm. The previous data set (K_d^{ref}) had a 7-year time span (1998–2004) to calculate a climatological year from SeaWiFS observations. Moreover, another advantage to the previous K_d model input is the use of a product derived for regional purposes only, i.e. the Mediterranean Sea, which has been in the past already seen as a bio-optically anomalous region and as such needs algorithms that vary from global ones (see Organelli et al., 2017 and references therein).

In Lazzari et al. (2012) the light attenuation term was derived from SeaWiFS data of seasonal climatological measurements for the period between 1998 and 2004. As already discussed in the aforementioned paper, such an approach could introduce uncertainties due to several

Table 3

Basin-scale match-up between model outputs (from S^{ref} , $S^{new(clim)}$ and S^{new}) and available BGC-Argo floats, expressed for season (N is the number of match-ups) with statistical parameters (Bias [mg m^{-3}], RMSE [mg m^{-3}] and correlation coefficient).

Season	N	Bias			RMSE			CORR		
		S^{ref}	$S^{new(clim)}$	S^{new}	S^{ref}	$S^{new(clim)}$	S^{new}	S^{ref}	$S^{new(clim)}$	S^{new}
Winter	30 569	-0.044	-0.044	-0.045	0.128	0.128	0.128	0.636	0.642	0.650
Spring	33 015	0.030	0.029	0.023	0.178	0.174	0.168	0.617	0.635	0.674
Summer	28 470	0.028	0.033	0.030	0.146	0.152	0.148	0.570	0.539	0.569
Autumn	18 880	-0.028	-0.028	-0.025	0.102	0.102	0.105	0.690	0.693	0.675

reasons: firstly, the use of K_d for only one wavelength (490 nm) is chosen in order to parametrize the diffuse attenuation for the whole visible range (400–700 nm), namely $K_d(PAR)$. Secondly, by extrapolating the constant value calculated for the first optical depth (on average between 15 and 35 m in the Mediterranean; see D'Ortenzio and Ribera d'Alcalà, 2009) along the entire water column, the depth variability of K_d is *a priori* neglected. Nevertheless, constraining biogeochemical models to satellite-derived products proved to help capturing the west-east gradient of chlorophyll dynamics in terms of surface values and DCM depth in the Mediterranean Sea (Lazzari et al., 2012), with successful implementations also for operational purposes (Lazzari et al., 2010; Salon et al., 2019).

Our results show that the upgrade of the K_d has a double impact: increasing spatial and temporal variability of the chlorophyll dynamics in the ecosystem and modifying vertical distribution (e.g., DCM depth) and magnitude of chlorophyll. While the first aspect is quite obvious, the second is much more difficult to interpret since the non-linear response of phytoplankton to the interaction between light, nutrient resource availability and top-down control along the water column, and the effect of the vertical mixing regimes.

The impact of the upgraded model on spatial variability was initially discussed with K_d maps (Fig. 3), where major differences were spotted in western regions during late winter/early spring months. Chl maps showed higher values in western sub-basins at the surface during spring (Fig. 4), at 50 m persisting also in summer months (Fig. 5), followed by an enhancement in eastern parts at 100 m during summer and autumn, the last two cases corresponding to the period and depth of DCM formation in the regions. Generally, a non-linear relationship between K_d change and impact on surface chlorophyll is observed. While a positive (negative) change of K_d causes decrease (increase) of chlorophyll (i.e., March in the south-(north-)western subbasins) as a response of lower (higher) light availability in the surface layer, the same K_d change causes a negative change in chlorophyll in the whole area in April. An increase of the top-down control of phytoplankton biomass is the response after the increased production in a region of high vertical mixing (not shown). On the other hand, another mechanism is possibly acting in the ultra-oligotrophic eastern Levantine areas. The winter decrease of surface chlorophyll (Fig. 4, first row and Fig. A.11) concurrent with the decrease of K_d reflects a complex interaction along the water column dynamics where the higher light availability at 100 depth causes an increase of chlorophyll (Figs. 6 and A.12) which in turn consumes nutrients and increases the nutrient depletion at surface in areas with weak vertical mixing regime. This spatially heterogeneity most likely results from a complex interaction of K_d with the entire water column, where the vertical mixing regime in turn may cause non-linear responses of the surface Chl dynamics on K_d . A non-linear response is widely observed also at depth (as in Fig. 5), as a result of the model's non-linearity (i.e. photoacclimation vs. photosynthesis processes).

In fact, while an increase of light at depth causes a deepening of the DCM and vice versa (Fig. 7), the response of the chlorophyll concentration at different depths to the change of K_d is mediated by the water column dynamics. For example, the increase of K_d in June (Fig. 3) causes an increase of chlorophyll at 100 m in western sub-basins (consistently with the deepening of the DCM) but a decrease of chlorophyll in the eastern sub-basins (as a response of the low

nutrient flux reaching a layer above a deepened DCM in a weak vertical mixing regime). Thus, different shapes of chlorophyll profiles are expected to emerge as the result of multiple factors acting with different intensity in the regions of the Mediterranean Sea (Barbieux et al., 2019). However, it must be noted that our results, while satisfactorily describe the basin-wide gradient of the chlorophyll field, might lack a full realistic relationship between K_d and chlorophyll: actually, the self-shading process is not considered, and specific mechanisms related to resource competition (including light) impacting chlorophyll and nutrient distribution (Tilman, 1980) could be oversimplified.

Results further demonstrated that with the use of K_d^{new} , the DCM depth increased throughout the entire basin of about 2%–5% on average (Fig. 9), especially in late summer/early autumn months (Fig. 7c). Moreover, an increase of the interannual variability of the DCM depth was observed, both as increment of the related statistical indicator (Fig. 7d) and as increment of the mean latitudinal DCM depth values range (Fig. 8). DCM depth thus proves to be a good indicator to follow a consistent response between light and the water column biogeochemical dynamics. Similar increment in magnitude and mean latitudinal values range were found considering the total chlorophyll biomass per area in the 0–200 m layer. The enhancement of the interannual variability of the chlorophyll field at depth, on a monthly scale, was assessed showing the increase of the related statistical indicators at 100 m (Fig. A.12).

The average effect on DCM characteristics, and in general over the mean Chl vertical profile, of the updated diffuse attenuation coefficient was also quantified examining the match-up of our simulations with a recently acquired BGC-Argo floats data set. Our results showed that the CMEMS product quality indicators improve with the use of K_d^{new} , especially in spring (Bias -24%, RMSE -6%, correlation +9%) and in autumn (Bias -10%). When we observe a quality drop (as in summer RMSE), the use of the interannually variable K_d lessens the worsening effect related to the sensor/algorithm change. This result is particularly strategic for the specific production of reanalysis in the CMEMS framework (see Teruzzi et al., 2014a). In fact, building a biogeochemical reanalysis simulation (see Fennel et al., 2019) means to gather a large series of information and data that set the physical forcing, the initial and the boundary conditions, as well as observations for the validation assessment. Thus, considering the complexity of a reanalysis production, the upgrade of even a single element, as K_d , which may bring a small relative improvement of quality, is important.

5. Conclusions

Light propagation along the water column is one of the major drivers in shaping the vertical variability of the ecosystems. Our study was framed with two main targets: on one side evaluating how a new data set of diffuse attenuation coefficient K_d retrieved from satellite changes the temporal and spatial variability of the chlorophyll field and the deep chlorophyll maximum (DCM) features, assessing both satellite sensor and algorithm upgrade and the inclusion of the interannual variability. On the other side, estimating how this new K_d data set affects the MedBFM model skill according to CMEMS guidelines, by evaluating the surface chlorophyll product quality and comparing model profiles with a quality-controlled BGC-Argo floats data set. The use of the new K_d data set results in an increase in chlorophyll

variability both in terms of spatial patterns and temporal variability, particularly in the deepest part of the euphotic layer. Consequently, also the DCM dynamics show an increased variability. Furthermore, the updated model configuration shows a slightly higher skill compared to the reference one in the match-up analysis with the BGC-Argo data set. The role played by the introduction of the interannual variability of K_d in the model improved performance appears larger than the impact due to the sensor/algorithm change, both with a direct effect (as in spring and autumn), and also with an indirect effect, mitigating the quality worsening related to the change in the satellite sensor (as in summer).

The presented approach therefore constitutes a simple, but efficient step in the path of possible model upgrades, showing how remote sensing products can effectively improve phytoplankton dynamics in biogeochemical model reanalyses. Results shown in this paper are especially addressed to ecological modellers who lack a more complex representation of the optical properties.

Our work showed the importance of including more realistic optical forcing in biogeochemical modelling. Though our model integrates the diffuse attenuation coefficient (basically a remote sensing proxy), a further step forward would be the use of multi or hyperspectral modelling, which is designed to link radiometry data to inherent and apparent optical properties, aiming to include the radiative transfer theory into biogeochemistry.

CRediT authorship contribution statement

Elena Terzić: Methodology, Software, Validation, Formal analysis, Investigation, Writing - original draft, Visualization (within her Ph.D.), Data Curation, Writing - reviewing and editing. **Stefano Salon:** Supervision, Conceptualization, Methodology, Funding acquisition, Resources, Writing - reviewing and editing. **Gianpiero Cossarini:** Conceptualization, Methodology, Funding acquisition, Formal analysis, Writing - reviewing and editing. **Cosimo Solidoro:** Conceptualization, Methodology, Funding acquisition. **Anna Teruzzi:** Software, Visualization, Writing - reviewing and editing. **Arnau Miró:** Software, Visualization, Data curation. **Paolo Lazzari:** Resources, Funding acquisition, Formal analysis, Software, Writing - reviewing and editing, Supervision (during ET Ph.D.).

Declaration of competing interest

The authors declare that they have no known competing financial interests or personal relationships that could have appeared to influence the work reported in this paper.

Acknowledgements

This study has been conducted using EU Copernicus Marine Service Information. The authors thank Giorgio Bolzon (OGS) for the technical support provided in the MedBFM post-processing workflow. Elena Terzić and Arnau Miró grants were funded by the CMEMS, Italy contract for the Biogeochemistry Production Unit of the Mediterranean Sea Monitoring and Forecasting Centre and the CMEMS Service Evolution BIOPTIMOD³ project. CMEMS is implemented by Mercator Ocean International in the framework of a delegation agreement with the European Union.

All simulations were carried out at CINECA HPC facilities (Bologna, Italy) in the frame of ISCR projects MYMEDBIO (code: HP10C8HYKJ), ECOMED (code: HP10C1IXMA), and ECOMED2 (code: HP10C3FZCK).

Appendix A. Indicators of chlorophyll spatial and temporal variability

A statistical analysis of weekly Chl outputs from both simulations S^{ref} and S^{new} was performed to assess the impact of the updated diffuse attenuation coefficient on spatial and temporal scales separately. Initially, for each vertical level, the model output was spatially aggregated for each sub-basin k ($k = 1, 16$), obtaining sub-basin averages $Chl_m^k(j)$ and standard deviations $\sigma(Chl_m^k(j))$ for each month m ($m = 1, 12$) and for each year j between 1999 and 2015 ($j = 1, 17$).

Statistics in Figs. A.11 and A.12 are calculated following the equations reported below for the two simulations $sim = ref, new$ (note that the indices for each sub-basin k and month m are omitted for brevity):

$$\overline{M^{sim}} = \frac{1}{n_y} \sum_{j=1}^{n_y} Chl_m^k(j) \quad (A.1)$$

$$\sigma(M^{sim}) = \sqrt{\frac{1}{n_y} \sum_{j=1}^{n_y} (Chl_m^k(j) - \overline{M^{sim}})^2} \quad (A.2)$$

$$\overline{STD^{sim}} = \frac{1}{n_y} \sum_{j=1}^{n_y} \sigma(Chl_m^k(j)) \quad (A.3)$$

$$\sigma(STD^{sim}) = \sqrt{\frac{1}{n_y} \sum_{j=1}^{n_y} (\sigma(Chl_m^k(j)) - \overline{STD^{sim}})^2} \quad (A.4)$$

where n_y denotes the number of years of the two simulations. From the equations above, $\overline{M^{sim}}$ is the sub-basin's climatological month and $\sigma(M^{sim})$ its interannual variability; $\overline{STD^{sim}}$ is the sub-basin's climatological spatial variability and $\sigma(STD^{sim})$ its interannual variability.

Figs. A.11 and A.12 are organized as follows: top plots show the mean of the simulation with K_d^{new} (Eq. (A.1), panel a), the interannual variability of the mean (Eq. (A.2), panel b) and the interannual variability of the spatial variability (Eq. (A.4), panel c). Bottom plots follow the same metrics as the top ones, by taking the difference of the two simulations. The two standard deviations computed for S^{new} quantify the effect of K_d^{new} interannual variability on the spatially heterogeneous model outputs: a positive difference in $\sigma(M^{new})$ and $\sigma(STD^{new})$ in comparison with S^{ref} highlights the importance of using the interannual variable K_d^{new} in the reconstruction of the spatial heterogeneity from year to year.

Surface mean chlorophyll variability (Fig. A.11a), higher in the western basin and peaked during winter and spring months, is controlled by a strong seasonal cycle. The corresponding chlorophyll interannual variability $\sigma(M^{new})$ in Fig. A.11b follows similar seasonal and spatial patterns and amounts to up to 20% of the signal, especially for spring months in the western basin. The interannual variability of the sub-basin spatial heterogeneity $\sigma(STD^{new})$ displays a similar pattern to $\sigma(M^{new})$, resulting lower than 0.02 mg m^{-3} in most of the basin (Fig. A.11c).

Differences with S^{ref} are observed (Fig. A.11c) in western sub-basins in late winter and April, clearly positive in the northern part in March (as already discussed for Fig. 4); variations in surface interannual variability show a similar pattern with a decrease (increase) in the north-western (south-western) sub-basins during April (May).

At 100 m, the mean Chl exhibits the presence of the DCM both in the western and in the eastern basin from spring to early autumn (Fig. A.12a), as already observed in Fig. 8, with highest values reached in the Levantine sub-basins in late spring and in SWM1 and TYR1. Chl shows a composite pattern of interannual variability (Fig. A.12b and c), with the highest interannual variability during transition periods (i.e. spring and autumn), amounting to up to 0.06 mg m^{-3} . The comparison of S^{new} and S^{ref} clearly shows augmented mean (Fig. A.12d) and interannual variability, due to the introduction of the K_d^{new} , with both indicators $\sigma(M^{new})$ and $\sigma(STD^{new})$ presenting positive differences up to 40%, specifically in summer in western sub-basins and in April in Levantine (Fig. A.12e, f).

³ <https://www.mercator-ocean.fr/en/portfolio/bioptimod/>.

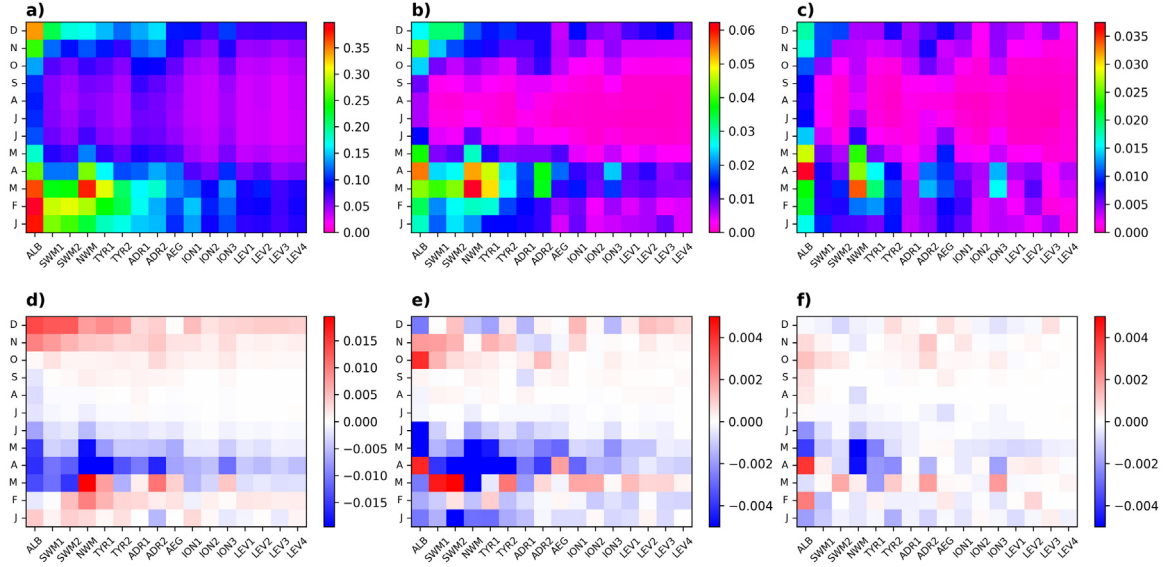


Fig. A.11. Top: Surface Chl monthly mean (a) and standard deviation calculated with S^{new} , first with mean as the statistical indicator (b), and then with standard deviation (c), i.e. $\sigma(M^{new})$ and $\sigma(STD^{new})$ respectively. Bottom: Surface Chl monthly mean (d) and standard deviation ($\sigma(M)$ and $\sigma(STD)$); (e) and (f) of the difference between S^{new} and S^{ref} . The order of sub-basin in the x -axis roughly follows the eastward direction.

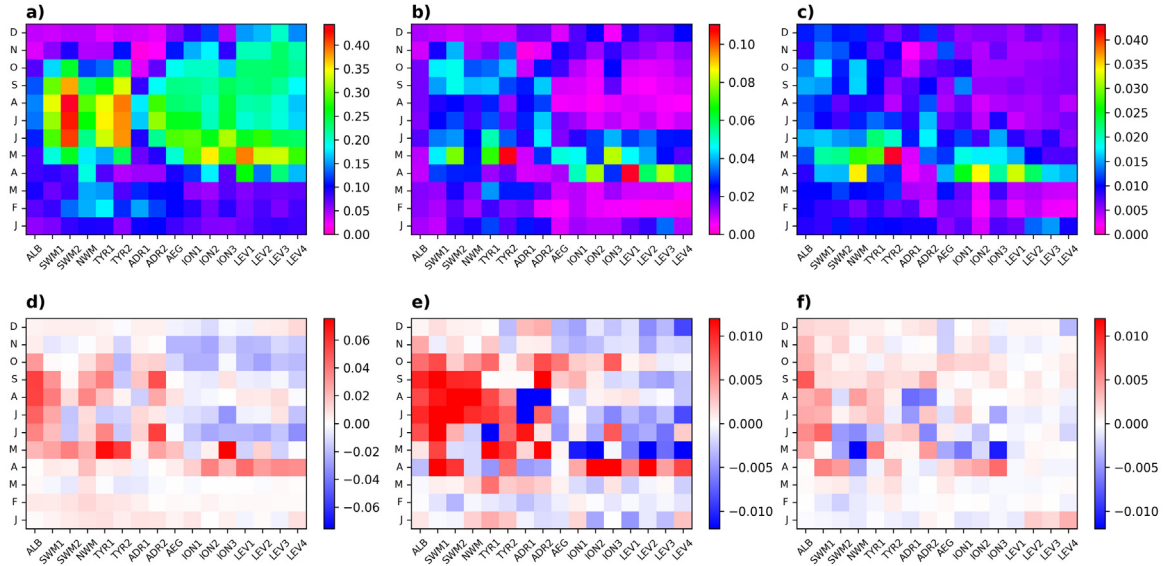


Fig. A.12. Top: Chl monthly mean at 100 m depth (a) and standard deviation calculated with S^{new} , first with mean as the statistical indicator (b), and then with standard deviation (c), i.e. $\sigma(M^{new})$ and $\sigma(STD^{new})$ respectively. Bottom: Surface Chl monthly mean (d) and standard deviation ($\sigma(M)$ and $\sigma(STD)$); (e) and (f) of the difference between S^{new} and S^{ref} . The order of sub-basin in the x -axis roughly follows the eastward direction.

At 50 m depth (figures not shown), a noticeable signal in mean chlorophyll patterns is observed during the period of DCM formation in western basin, the latter also characterized by a larger spatial and temporal variability during spring, when compared to eastern sub-basins. The updated K_d coefficient does not severely affect S^{new} , except for a slight increase in interannual variability in NWM, SWM1 and SWM2 in early spring.

The effect of K_d^{new} within the euphotic layer is to generally increase both the spatial and interannual variability of the post-bloom chlorophyll field (i.e. from April to October in the western basin and in April in the eastern basin) with increasing depth.

Appendix B. Statistical quality indicators

The product quality was evaluated with three statistical parameters: Bias, root mean square error (RMSE) and the Pearson correlation

coefficient (ρ), that were calculated following Eqs. (B.1) to (B.3):

$$Bias = \frac{1}{n} \sum_{i=1}^n (x_i - y_i) \quad (B.1)$$

$$RMSE = \sqrt{\frac{1}{n} \sum_{i=1}^n (x_i - y_i)^2} \quad (B.2)$$

$$\rho = \frac{cov(x, y)}{\sigma_x \sigma_y} \quad (B.3)$$

where

$$cov(x, y) = \frac{\sum_{i=1}^n (x_i - \bar{x})(y_i - \bar{y})}{n - 1} \quad (B.4)$$

In the above equations, x equals the Chl grid-point model output and y denotes Chl from the BGC-Argo floats; σ represents the standard deviation of the model/data values.

References

- Barbieux, M., Uitz, J., Gentili, B., de Fommervault, O.P., Mignot, A., Poteau, A., Schmechtig, C., Taillandier, V., Leymarie, E., Penkerch, C., et al., 2019. Bio-optical characterization of subsurface chlorophyll maxima in the mediterranean sea from a biogeochemical-argo float database. *Biogeosciences* 16 (6), 1321–1342.
- Bittig, H.C., Maurer, T.L., Plant, J.N., Wong, A.P., Schmechtig, C., Claustre, H., Trull, T.W., Udaya Bhaskar, T., Boss, E., Dall’Olmo, G., et al., 2019. A BGC-argo guide: Planning, deployment, data handling and usage. *Front. Mar. Sci.* 6, 502.
- Boldrin, A., Miserocchi, S., Rabitti, S., Turchetto, M., Balboni, V., Socal, G., 2002. Particulate matter in the southern adriatic and ionian sea: characterisation and downward fluxes. *J. Mar. Syst.* 33, 389–410.
- Bolzon, G., Cossarini, G., Lazzari, P., Salon, S., Teruzzi, A., Feudale, L., Solidoro, C., 2019. Mediterranean Sea Biogeochemical Analysis and Forecast (CMEMS MED-Biogeochemistry) [Data set]. Technical Report, Copernicus Monitoring Environment Marine Service (CMEMS), https://doi.org/10.25423/MEDSEA_ANALYSIS_FORECAST_BIO_006_014.
- Canu, D.M., Ghermandi, A., Nunes, P.A., Lazzari, P., Cossarini, G., Solidoro, C., 2015. Estimating the value of carbon sequestration ecosystem services in the mediterranean sea: An ecological economics approach. *Global Environ. Change* 32, 87–95.
- Christaki, U., Giannakourou, A., Van Wambeke, F., Grégori, G., 2001. Nanoflagellate predation on auto-and heterotrophic picoplankton in the oligotrophic mediterranean sea. *J. Plankton Res.* 23 (11), 1297–1310.
- Ciavatta, S., Kay, S., Brewin, R., Cox, R., Di Cicco, A., Nencioli, F., Polimene, L., Sammartino, M., Santoleri, R., Skákala, J., Tzapakis, M., 2019. Ecoregions in the mediterranean sea through the reanalysis of phytoplankton functional types and carbon fluxes. *J. Geophys. Res. Oceans* 124 (10), 6737–6759.
- Ciavatta, S., Kay, S., Saux-Picart, S., Butenschön, M., Allen, J., 2016. Decadal reanalysis of biogeochemical indicators and fluxes in the north west European shelf-sea ecosystem. *J. Geophys. Res. Oceans* 121 (3), 1824–1845.
- Ciavatta, S., Torres, R., Saux-Picart, S., Allen, J.L., 2011. Can ocean color assimilation improve biogeochemical hindcasts in shelf seas?. *J. Geophys. Res. Oceans* 116 (C12).
- Clementi, E., Pistoia, J., Escudier, R., Delrosso, D., Drudi, M., Grandi, A., Pinardi, N., 2019. Mediterranean Sea Analysis and Forecast (CMEMS MED-Currents 2016–2019). Technical Report, Copernicus Monitoring Environment Marine Service (CMEMS), URL: https://doi.org/10.25423/CMCC/MEDSEA_ANALYSIS_FORECAST_PHY_006_013_EAS4.
- Colella, S., Brando, V., Di Cicco, A., D’Alimonte, D., Forneris, V., Bracaglia, 2021. Ocean colour Production Centre, Quality Information Document of Ocean Colour Mediterranean and Black Sea Observation Product. Technical Report, Copernicus Monitoring Environment Marine Service (CMEMS).
- Cossarini, G., Querin, S., Solidoro, C., 2015. The continental shelf carbon pump in the northern adriatic sea (mediterranean sea): Influence of wintertime variability. *Ecol. Model.* 314, 118–134.
- Cullen, J.J., 2015. Subsurface chlorophyll maximum layers: enduring enigma or mystery solved?. *Ann. Rev. Mar. Sci.* 7, 207–239.
- Dolan, J., Claustre, H., Carlotti, F., Plounevez, S., Moutin, T., 2002. Microzooplankton diversity: relationships of tintinnid ciliates with resources, competitors and predators from the atlantic coast of Morocco to the eastern mediterranean. *Deep Sea Res. Part I: Oceanogr. Res. Pap.* 49 (7), 1217–1232.
- Doney, S.C., Lima, I., Moore, J.K., Lindsay, K., Behrenfeld, M.J., Westberry, T.K., Mahowald, N., Glover, D.M., Takahashi, T., 2009. Skill metrics for confronting global upper ocean ecosystem-biogeochemistry models against field and remote sensing data. *J. Mar. Syst.* 76 (1–2), 95–112.
- D’Ortenzio, F., Ribera d’Alcalá, M., 2009. On the trophic regimes of the mediterranean sea: a satellite analysis. *Biogeosciences* 6 (2), 139–148.
- Dutkiewicz, S., Hickman, A., Jahn, O., Gregg, W., Mouw, C., Follows, M., 2015. Capturing optically important constituents and properties in a marine biogeochemical and ecosystem model. *Biogeosciences* 12 (14), 4447–4481.
- Dutkiewicz, S., Hickman, A.E., Jahn, O., Henson, S., Beaulieu, C., Monier, E., 2019. Ocean colour signature of climate change. *Nature Commun.* 10 (1), 578.
- Ebenhoh, W., Baretta-Bekker, J., Baretta, J., 1997. The primary production module in the marine ecosystem model ERSEM II, with emphasis on the light forcing. *J. Sea Res.* 38 (3–4), 173–193.
- Estrada, M., Marrasé, C., Latasa, M., Berdalet, E., Delgado, M., Riera, T., 1993. Variability of deep chlorophyll maximum characteristics in the northwestern mediterranean. *Mar. Ecol. Progr. Ser.* 92, 289.
- Fennel, K., Gehlen, M., Brasseur, P., Brown, C.W., Ciavatta, S., Cossarini, G., Crise, A., Edwards, C.A., Ford, D., Friedrichs, M.A., et al., 2019. Advancing marine biogeochemical and ecosystem reanalyses and forecasts as tools for monitoring and managing ecosystem health. *Front. Mar. Sci.* 6.
- Foujols, M.-A., Lévy, M., Aumont, O., Madec, G., 2000. OPA 8.1 Tracer model reference manual. Technical Report, p. 39.
- Geider, R.J., MacIntyre, H.L., Kana, T.M., 1998. A dynamic regulatory model of phytoplankton acclimation to light, nutrients, and temperature. *Limnol. Oceanogr.* 43 (4), 679–694.
- Gregg, W.W., Friedrichs, M.A., Robinson, A.R., Rose, K.A., Schlitzer, R., Thompson, K.R., Doney, S.C., 2009. Skill assessment in ocean biological data assimilation. *J. Mar. Syst.* 76 (1–2), 16–33.
- Groom, S.B., Sathyendranath, S., Ban, Y., Bernard, S., Brewin, B., Brotas, V., Brockmann, C., Chauhan, P., Choi, J.-k., Chuprin, A., et al., 2019. Satellite ocean colour: current status and future perspective. *Front. Mar. Sci.* 6, 485.
- Hogan, R.J., Bozzo, A., 2018. A flexible and efficient radiation scheme for the ECMWF model. *J. Adv. Modelling Earth Syst.* 10 (8), 1990–2008.
- Lavigne, H., D’Ortenzio, F., d’Alcalá, M.R., Claustre, H., Sauzède, R., Gacic, M., 2015. On the vertical distribution of the chlorophyll a concentration in the mediterranean sea: a basin-scale and seasonal approach. *Biogeosciences* 12 (16), 5021–5039.
- Lazzari, P., Salon, S., Terzić, E., Gregg, W.W., D’Ortenzio, F., Vellucci, V., Organelli, E., Antoine, D., 2020. Assessment of the spectral downward irradiance at the surface of the mediterranean sea using the OASIM ocean-atmosphere radiative model. *Ocean Sci. Discuss.* 2020, 1–39. <http://dx.doi.org/10.5194/os-2020-108>, URL <https://os.copernicus.org/preprints/os-2020-108/>.
- Lazzari, P., Solidoro, C., Ibello, V., Salon, S., Teruzzi, A., Béranger, K., Colella, S., Crise, A., 2012. Seasonal and inter-annual variability of plankton chlorophyll and primary production in the mediterranean sea: a modelling approach. *Biogeosciences* 9 (1), 217.
- Lazzari, P., Solidoro, C., Salon, S., Bolzon, G., 2016. Spatial variability of phosphate and nitrate in the mediterranean sea: A modeling approach. *Deep Sea Res. Part I: Oceanogr. Res. Pap.* 108, 39–52.
- Lazzari, P., Teruzzi, A., Salon, S., Campagna, S., Calonaci, C., Colella, S., Tonani, M., Crise, A., 2010. Pre-operational short-term forecasts for mediterranean sea biogeochemistry. *Ocean Sci.* 6 (1), 25–39.
- Mattern, J.P., Song, H., Edwards, C.A., Moore, A.M., Fiechter, J., 2017. Data assimilation of physical and chlorophyll a observations in the californica current system using two biogeochemical models. *Ocean Model.* 109, 55–71. <http://dx.doi.org/10.1016/j.ocemod.2016.12.002>, URL: <http://www.sciencedirect.com/science/article/pii/S1463500316301470>.
- Mignot, A., Claustre, H., Uitz, J., Poteau, A., D’Ortenzio, F., Xing, X., 2014. Understanding the seasonal dynamics of phytoplankton biomass and the deep chlorophyll maximum in oligotrophic environments: A bio-argo float investigation. *Glob. Biogeochem. Cycles* 28 (8), 856–876.
- Morel, A., Gentili, B., Claustre, H., Babin, M., Bricaud, A., Ras, J., Tiede, F., 2007a. Optical properties of the “clearest” natural waters. *Limnol. Oceanogr.* 52 (1), 217–229.
- Morel, A., Huot, Y., Gentili, B., Werdell, P.J., Hooker, S.B., Franz, B.A., 2007b. Examining the consistency of products derived from various ocean color sensors in open ocean (case 1) waters in the perspective of a multi-sensor approach. *Remote Sens. Environ.* 111 (1), 69–88.
- Morel, A., Maritorena, S., 2001. Bio-optical properties of oceanic waters: A reappraisal. *J. Geophys. Res. Oceans* 106 (C4), 7163–7180.
- Moutin, T., Raimbault, P., 2002. Primary production, carbon export and nutrients availability in western and eastern mediterranean sea in early summer 1996 (MINOS cruise). *J. Mar. Syst.* 33, 273–288.
- O’Reilly, J.E., Maritorena, S., Siegel, D.A., O’Brien, M.C., Toole, D., Mitchell, B.G., Kahru, M., Chavez, F.P., Strutton, P., Cota, G.F., et al., 2000. Ocean color chlorophyll a algorithms for seawifs, OC2, and OC4: Version 4, SeaWiFS postlaunch calibration and validation analyses, part 3. pp. 9–23.
- Organelli, E., Claustre, H., Bricaud, A., Barbieux, M., Uitz, J., D’Ortenzio, F., Dall’Olmo, G., 2017. Bio-optical anomalies in the world’s oceans: An investigation on the diffuse attenuation coefficients for downward irradiance derived from biogeochemical argo float measurements. *J. Geophys. Res. Oceans* 122 (5), 3543–3564.
- Organelli, E., Claustre, H., Bricaud, A., Schmechtig, C., Poteau, A., Xing, X., Prieur, L., D’Ortenzio, F., Dall’Olmo, G., Vellucci, V., 2016. A novel near-real-time quality-control procedure for radiometric profiles measured by bio-argo floats: Protocols and performances. *J. Atmos. Ocean. Technol.* 33 (5), 937–951.
- Salon, S., Cossarini, G., Bolzon, G., Feudale, L., Lazzari, P., Teruzzi, A., Solidoro, C., Crise, A., 2019. Novel metrics based on biogeochemical argo data to improve the model uncertainty evaluation of the CMEMS mediterranean marine ecosystem forecasts. *Ocean Sci.* 15 (4), 997–1022. <http://dx.doi.org/10.5194/os-15-997-2019>, <https://www.ocean-sci.net/15/997/2019/>.
- Simon, E., Samuelsen, A., Bertino, L., Mouisset, S., 2015. Experiences in multiyear combined state-parameter estimation with an ecosystem model of the North Atlantic and Arctic Oceans using the ensemble Kalman filter. *J. Mar. Syst.* 152, 1–17.
- Siokou-Frangou, I., Christaki, U., Mazzocchi, M.G., Montresor, M., d’Alcalá, M.R., Vaqué, D., Zingone, A., 2010. Plankton in the open mediterranean sea: a review. *Biogeosciences* 7 (5), 1543–1586. <http://dx.doi.org/10.5194/bg-7-1543-2010>.

- Skákala, J., Bruggeman, J., Brewin, R.J., Ford, D.A., Ciavatta, S., 2020. Improved representation of underwater light field and its impact on ecosystem dynamics: a study in the north sea. *J. Geophys. Res. Oceans* e2020JC016122.
- Song, H., Edwards, C.A., Moore, A.M., Fiechter, J., 2016a. Data assimilation in a coupled physical-biogeochemical model of the california current system using an incremental lognormal 4-dimensional variational approach: Part 1-model formulation and biological data assimilation twin experiments. *Ocean Model.* 106, 131–145. <http://dx.doi.org/10.1016/j.ocemod.2016.04.001>, URL: <http://www.sciencedirect.com/science/article/pii/S1463500316300063>.
- Song, H., Edwards, C.A., Moore, A.M., Fiechter, J., 2016b. Data assimilation in a coupled physical-biogeochemical model of the california current system using an incremental lognormal 4-dimensional variational approach: Part 2-joint physical and biological data assimilation twin experiments. *Ocean Model.* 106, 146–158. <http://dx.doi.org/10.1016/j.ocemod.2016.09.003>, URL: <http://www.sciencedirect.com/science/article/pii/S1463500316300919>.
- Song, H., Edwards, C.A., Moore, A.M., Fiechter, J., 2016c. Data assimilation in a coupled physical-biogeochemical model of the california current system using an incremental lognormal 4-dimensional variational approach: Part 3-assimilation in a realistic context using satellite and in situ observations. *Ocean Model.* 106, 159–172. <http://dx.doi.org/10.1016/j.ocemod.2016.06.005>, URL: <http://www.sciencedirect.com/science/article/pii/S1463500316300555>.
- Teruzzi, A., Bolzon, G., Cossarini, G., Lazzari, P., Salon, S., Crise, A., Solidoro, C., 2014a. Mediterranean Sea Reanalysis (CMEMS MED-Biogeochemistry 1999-2015). Technical Report, Copernicus Monitoring Environment Marine Service (CMEMS), https://doi.org/10.25423/MEDSEA_REANALYSIS_BIO_006_008.
- Teruzzi, A., Bolzon, G., Salon, S., Lazzari, P., Solidoro, C., Cossarini, G., 2018. Assimilation of coastal and open sea biogeochemical data to improve phytoplankton simulation in the mediterranean sea. *Ocean Model.* 132, 46–60.
- Teruzzi, A., Dobricic, S., Solidoro, C., Cossarini, G., 2014b. A 3-d variational assimilation scheme in coupled transport-biogeochemical models: Forecast of mediterranean biogeochemical properties. *J. Geophys. Res. Oceans* 119 (1), 200–217.
- Terzić, E., Lazzari, P., Organelli, E., Solidoro, C., Salon, S., D'Ortenzio, F., Conan, P., 2019. Merging bio-optical data from biogeochemical-argo floats and models in marine biogeochemistry. *Biogeosciences* 16 (12), 2527–2542.
- Tilman, D., 1980. Resources: a graphical-mechanistic approach to competition and predation. *Amer. Nat.* 116 (3), 362–393.
- Turley, C., Bianchi, M., Christaki, U., Conan, P., Harris, J., Psarra, S., Ruddy, G., Stutt, E., Tselepidis, A., Van Wambeke, F., 2000. Relationship between primary producers and bacteria in an oligotrophic sea—the mediterranean and biogeochemical implications. *Mar. Ecol. Prog. Ser.* 193, 11–18.
- Vichi, M., Cossarini, G., Gutierrez, M., Lazzari, P., Lovato, T., Mattia, G., Masina, S., McKiver, W., Pinardi, N., Solidoro, C., Zavatarelli, M., 2013. The Biogeochemical Flux Model (BFM): Equation Description and User Manual. BFM Report series 1, BFM version 5 (BFM-V5), Bologna, Italy, <http://bfm-community.eu>.
- Vichi, M., Pinardi, N., Masina, S., 2007. A generalized model of pelagic biogeochemistry for the global ocean ecosystem. Part I: Theory. *J. Mar. Syst.* 64 (1), 89–109.
- Volpe, G., Colella, S., Brando, V.E., Forneris, V., La Padula, F., Cicco, A.D., Sammartino, M., Bracaglia, M., Artuso, F., Santoleri, R., 2019. Mediterranean ocean colour level 3 operational multi-sensor processing. *Ocean Sci.* 15 (1), 127–146.
- Volpe, G., Pitarch, J., Colella, S., Brando, V., Forneris, V., Bracaglia, M., Benincasa, M., 2017. ocean colour Production Centre, Quality Information Document of Ocean Colour Mediterranean and Black Sea Observation Product v1.5. Technical Report, Copernicus Monitoring Environment Marine Service (CMEMS).
- Xing, X., Briggs, N., Boss, E., Claustre, H., 2018. Improved correction for non-photochemical quenching of in situ chlorophyll fluorescence based on a synchronous irradiance profile. *Optics Express* 26 (19), 24734–24751.